PAPER

Check for updates

Reversible magnetic soft actuators made of thermoplastic polyurethane and yttrium iron garnet†

Mariana Martins da Silva, [ID] *‡[a] Alejandro Rivelles, [ID] [b] José A. Covas, [ID] [a] Maria C. Paiva [ID] [a] and Mariana P. Proença [ID] *[b]

Imparting magnetic properties to elastomeric polymers opens up possibilities to generate intelligent materials that may mimic complex biological systems, allowing reversible deformations under a magnetic stimulus. Remotely triggered soft actuators made of thermoplastic polyurethane (TPU) and yttrium iron garnet, $Y_3Fe_5O_{12}$ (YIG), were prepared through micro melt compounding, a solvent-free and environmentally friendly scalable technique. The magnetic composites (mTPU) present a good interface between particles and the matrix while maintaining the elastomeric behaviour characteristic of TPU. Using a permanent magnet, the magnetomechanical behaviour of mTPU, with two different shapes and thicknesses, led to reversible bending at room temperature with a fast response time. Initial displacements at 100 Oe for a 500 μm thick tape and 85 Oe for a 150 μm thick tape are recorded. Thinner tapes enable more freedom in movement and have higher sensitivity to external magnetic fields, needing lower magnetic forces (around 38 times lower) for bending than the thicker tapes, that in turn allow for a more precise control. A switch actuator, composed of an mTPU/Au bi-layer, was developed to quickly open or close an electrical circuit upon exposure to a magnetic field.

1. Introduction

Currently, considerable attention is being given to lightweight and flexible soft actuators that are responsive to external stimuli. Their response manifests itself through significant deformations in their physical structure, making them highly versatile for various applications. Due to their low density, exceptional flexibility, simple fabrication, and the possibility of compounding, polymers and gels offer abundant design possibilities for the development of soft actuators.[1,2] Among the many fields that benefit from innovation in soft actuators are targeted drug delivery systems,[3,4] tissue engineering,[3,5] flexible electronics,[6,7] and soft robotic components.[2,8] Ongoing research demonstrates the vast potential of this class of materials, moving towards mechanisms that can display remote actuation and complex shape deformations.

[a]Institute for Polymers and Composites, University of Minho, Campus of Azurém, GuimarãesPortugal. E-mail: mmsilva@dep.uminho.pt
[b]ISOM and Departamento de Electrónica Física, Universidad Politécnica de Madrid, Ava. Complutense 30, Madrid, E-28040, Spain. E-mail: mariana.proenca@upm.es
†Electronic supplementary information (ESI) available. See DOI: https://doi.org/10.1039/d5lp00021a
‡Present address: School of Mechanical and Aerospace Engineering, Queen's University Belfast, Belfast, United Kingdom.

Polyurethane (PU) has been actively researched as a shape-memory polymer (SMP) owing to the presence of soft and hard polymer segments.[9–11] On its own, PU can deform either by direct heat stimuli, through the thermal activation of dynamic covalent bonds,[12] or in response to a solvent.[13] Adding fillers to produce PU composites can result in actuation triggered by other stimuli, such as electrical,[14,15] optical,[14–16] or magnetic, removing the need to control the local temperature for actuation.

Magnetically triggered polymer composites have the advantage of remote actuation.[17,18] Several works in the literature report the design of PU composites with magnetic particles to produce magnetic SMPs, the most common filler being magnetite (Fe_3O_4).[19–30] The actuation mechanism of such SMPs relies on applying an alternating magnetic field that heats the magnetic particles, with the magnetic field becoming an indirect source of heat capable of generating eddy currents in an electrically conductive material. In turn, the generated (inductive) heat heats the polymer and, with sufficient heat transfer, the polymer chains relax, leading to a mechanical deformation.[31,32] Other magnetic particles, such as nickel–zinc ferrite,[33] have been used to produce magnetic SMPs, whose actuation mechanism is also based on inductive heating (magnetothermal mechanism).

A magnetomechanical actuation mechanism can also be obtained for polymer/magnetic particle composite (mP) soft actuators. This actuation response depends on how $\vec{H}$ changes

the magnetic moment of the fillers embedded in the mP. Magnetomechanical actuation of PU composites has been achieved with the addition of Fe_3O_4,[34] carbonyl iron (Fe (CO)$_5$)[35,36] at a minimum applied field of 0.5 kOe for sample bending,[35] manganese ferrite ($MnFe_2O_4$) resulting in bending of samples between applied fields of 0.15–0.30 kOe,[37] and recently by adding strontium hexaferrite ($SrFe_{12}O_{19}$) particles enabling actuation under both direct and alternating currents.[38] However, most of these mPs are produced by solvent casting methods, recurring to the use of tetrahydrofuran to homogeneously distribute the magnetic fillers in the polymer.[35–37] Aiming at a cleaner and more environmentally friendly large-scale production, it is mandatory to produce composites based on solvent-free techniques such as melt-mixing routes, to disperse particulate fillers in thermoplastic polymer matrices.[19,38] A chronological sequence of the magnetic fillers used in the fabrication of magnetic soft actuators with a thermoplastic polyurethane (TPU) matrix (*i.e.* remouldable, recyclable, and reusable), along with their mechanism of actuation, filler content, and processing route, is illustrated in Fig. 1.

Yttrium iron garnet (YIG) is an insulating ferrimagnet, with low magnetization, presenting very low magnetic losses at high frequencies (radio and microwave). Typically used in microwave (MW) devices due to its small dielectric loss,[39] YIG has been little explored as a filler in polymer matrices. Table 1 summarizes previous studies on polymer composites with YIG. Incorporation of YIG into polymers has been reported to improve dielectric properties for high-frequency and electromagnetic shielding applications,[40–44] to prepare magnetic bioseparators,[45] and to produce a flexible collagen composite, capable of being attracted by a permanent magnet.[46] In comparison with other magnetic particulate fillers, YIG has the advantage of being a highly insulating magnetic material, thus, not responding to electrical interference. Its low coercivity and low remanence, together with its small saturation field, enable a fast orientation of the magnetic domains within the grains, thus allowing actuation at low $\vec{H}$.

The low magnetic losses of YIG can be of particular interest to develop actuators with an efficient energy transfer and not liable to be disrupted by external electrical noise due to its

Table 1 Polymer composites with yttrium iron garnet

Polymer	YIG (wt%)	Year	Ref.
Poly(methyl methacrylate)	10–40	2008	40
Thermoplastic ER182	30	2010	41
Collagen	42.5–64.6	2010	46
Polyvinylidene fluoride	6–13	2012	42
Cellulose acetate	5–20	2014	45
Polyaniline	—	2018	43
Polypyrrole	11–80	2019	44
Epoxy	1–20	2020	47

insulating nature. Therefore, composites with YIG are good candidates for high precision and control applications, with simplified circuit design needs and reduced complexity capable of operating at high frequencies. In comparison, magnetic fillers such as Fe_3O_4, $MnFe_2O_4$, and $NiZnFe_2O_4$ are semiconducting, have higher magnetic losses, and are less efficient for high-frequency applications. Furthermore, the low density of YIG can help in creating lightweight composites, which is a significant factor in fields like the aerospace and automotive industries. YIG has a relatively low saturation magnetization compared to other magnetic materials, such as ferrites or rare-earth magnets. This means that, although it is a good material for high-frequency applications, it may not generate as strong magnetic fields or forces as other materials. This could limit its ability to produce large actuation forces in low-field applications. Adequate processing routes that ensure good dispersion of particulate fillers, avoiding agglomeration and promoting a homogeneous distribution, are therefore necessary to ensure proper property transfer from YIG particles while preserving the mechanical and viscoelastic properties of the polymer matrix.

The present work describes a solvent-free and scalable processing route to produce thermoplastic PU (TPU) composites with YIG (mTPU), by using a micro-compounder that promotes the homogeneous mixing of the YIG particles in the polymer melt. The method provides an environmentally friendly technique to prepare magnetomechanical soft actuators based on TPU and embedded sol–gel synthesised YIG particles. The
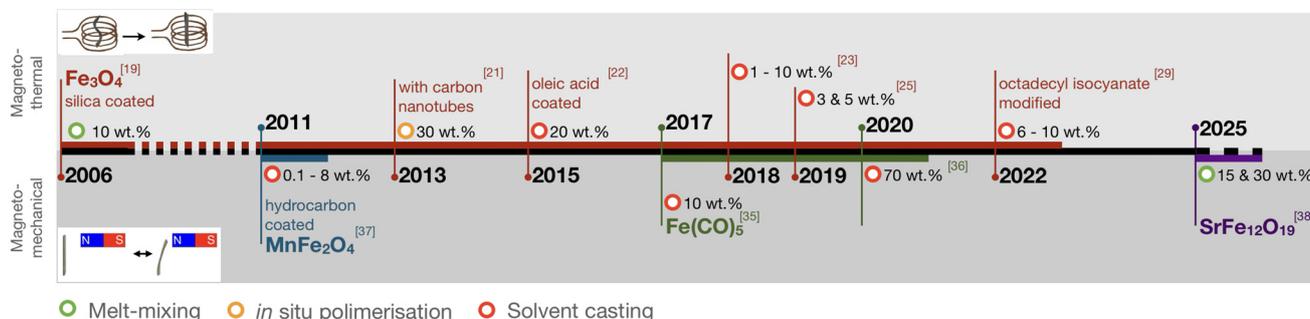
Fig. 1 Chronological overview of magnetic soft actuators, produced with a TPU matrix. The timeline is divided distinguishing between magnetothermal (top) and magnetomechanical (bottom) actuation mechanisms. Open circles, in different colours, denote the different processing methods.

structure and morphology of YIG powder and composites are analysed, as well as the thermomechanical properties of the composites. The magnetomechanical behaviour of mTPU with different thicknesses and shapes is successfully evaluated with the application of a magnetic field using permanent magnets. Their possible use as a soft switch actuator in a simple circuit is achieved through the assembly of a bi-layer structure of mTPU/Au.

2. Experimental

2.1. Synthesis of YIG powder

YIG particles were synthesised by a sol–gel method as described in the literature.[48–50] The pH and calcination step were selected according to previous studies, envisioning maximum saturation magnetization (M_s). Magnetic hysteresis loops and M_s of commercial and sol–gel synthesised YIG powders (at pH 2 and pH 10) are shown in the ESI (Fig. S1 and Table S1†), before and after calcination at 1000 °C.

Y(NO$_3$)$_3$·6H$_2$O (99.9%, Acros Organics, Geel, BE, lot: A0432222) and Fe(NO$_3$)$_3$·9H$_2$O (Fisher Scientific, NH, USA, lot: 2030874) were used as precursors in a 3:5 molar ratio of Y:Fe. Citric acid (C$_6$H$_8$O$_7$, PanReac, Barcelona, ES, lot: 0002077965) was used as a chelating agent in a 1:1 molar ratio of C$_6$H$_8$O$_7$:metals. The reagents were dissolved in ultra-pure H$_2$O (18 MΩ cm, 21 °C) under magnetic stirring (200 RPM). An initial solution with pH 1 was obtained. The pH was adjusted with an NH$_3$ solution (28–30%, EMSURE® Supelco, PA, USA), and the reaction was carried out after pH adjustment at 110 °C until a gel was formed (~21 h). The brown powder obtained was further calcined at 1000 °C for 3 hours in a muffle furnace, resulting in a green-coloured powder. This powder was ground with a mortar prior to characterisation and compounding.

2.2. Preparation of soft magnet polymer composites

The polymer matrix used was thermoplastic polyurethane (TPU) Desmopan 3360A, from Covestro, Leverkusen, Germany. The TPU pellets were dried for 4 h at 80 °C in a vacuum oven before the preparation of the composite. The YIG powders used were synthesized by the sol–gel method at pH 2, and calcined. The TPU–YIG composites were prepared by melt mixing on a micro-compounder Xplore MC 15, Xplore Instruments, Sittard, The Netherlands. The TPU and YIG were fed at a 90:10 (w/w) ratio (TPU:YIG). The micro-compounder is equipped with two non-intermeshing co-rotating conical screws and a recirculating channel (thus allowing control of the residence time). The composites were prepared at 190 °C at a screw speed of 150 rpm, and the melt was recirculated for 10 min, as described by da Silva et al.[38] The TPU–YIG (mTPU) filament was collected and pelletized. Sheets of mTPU with 500 and 150 μm thicknesses were prepared by compression moulding at 190 °C, under a pressure of 20 tons, for 10 min.

2.3. Characterisation of the structural properties

The crystalline structure of the YIG powder was evaluated by X-ray diffraction (XRD) and Raman spectroscopy. XRD patterns were acquired with an AXS D8 Discover diffractometer (Bruker, MA, USA), using Cu-K$_\alpha$ radiation (λ = 1.54060 Å). The analysis was carried out in the $\theta/2\theta$ configuration, at room temperature, in the range of 10° to 80°, with a step size of 0.02° and an integration time of 1 s per step. The crystallite grain size (L) was calculated using Scherrer's equation,

$$L = \frac{k \cdot \lambda}{\beta \cdot \cos(\theta)} \tag{1}$$

with a shape factor k of 0.9 and β being the full width at half maximum (FWMH) of the peak, in rad, at the peak position θ, in rad. The peaks were fitted with a Gauss function using OriginLab2024 software. Raman spectra of YIG powder and polymer composites were collected with a Horiba LabRAM HR Evolution system coupled to a CCD detector (Horiba, Kyoto, JP) and a confocal microscope, with 50× and 100× objectives and the confocal hole set to 100 μm. YIG powder spectra were collected with a 532 nm laser, in the range of 100–800 cm^{-1}, with a grating of 600 gr mm^{-1}. The 100× objective was used for the powder, with the ND filter set to 10% and a 15 s acquisition time with 5 accumulations. The mTPU composites were analysed with a 50× objective, and the ND filter was set to 50%, with a 15 s acquisition time and 10 accumulations. Peak positions of the spectra were obtained by fitting a Gaussian/Lorentzian function using LabSpec 6 software.

2.4. Morphology characterisation

The morphology and chemical composition of the YIG powder were analysed by scanning electron microscopy (SEM, FEI Inspect F50 microscope) and energy-dispersive X-ray spectroscopy (EDS, Oxford Instruments). The morphology of the cross-section of composites was analysed by SEM (Nano SEM– FEI Nova 200), with an integrated EDAX–Pegasus X4M under high vacuum (1.0 nm at 15 kV resolution), with TDL and ETD detectors, after coating cryofractured (immersed in liquid N$_2$) samples with Au–Pd (80–10 wt%). Digital images of the mTPU/Au bi-layer were obtained with a Leica DMS 1000 low-to-mid range magnification digital microscope.

2.5. Thermal and thermomechanical properties

Thermograms of the composites and neat TPU were recorded with a TGA Q500 (T.A. Instruments®, DE, USA), with a weighing precision of ±0.01% and 0.1 μg sensitivity at a heating rate of 10 °C min^{-1}, from 40 °C to 700 °C, under a N$_2$ atmosphere in a platinum crucible.

A TTDMA (Triton Technology, Grantham, UK) equipped with a 1 L Dewar and a TTDMA AutoCryo Type 2 for cooling with liquid nitrogen were used to perform dynamic mechanical analysis (DMA) in tensile mode, with a 5 mm gauge length. The frequency was set to 1 Hz with a displacement amplitude of 0.02 mm, in the temperature range from −80 °C to 150 °C, at a heating rate of 2 °C min^{-1}. The elastic modulus (E') values were obtained at 0, 25, and 37 ± 0.4 °C. The values presented for the glass transition temperature (T_g) were collected from the maximum of the tangent of delta curve (tan δ).

© 2025 The Author(s). Published by the Royal Society of Chemistry

RSC Appl. Polym., 2025, **3**, 865–874 | **867**

2.6. Magnetic properties

Magnetic hysteresis loops were obtained with a vibrating sample magnetometer (VSM) LakeShore Controller Model 7304 (Lake Shore Cryotronics Inc., Westerville, OH, USA), at room temperature. In-plane magnetic fields of up to 10 kOe were applied to fully saturate the samples and the field steps were adjusted to obtain smooth hysteresis loops. Before magnetic measurements, small amounts of YIG powder (Table S1, ESI†) were weighed on a microbalance on top of a ~2 × 2 cm^2 square Teflon tape and then wrapped and flattened, forming small disk-shaped (~4 mm in diameter) Teflon samples filled with YIG powder. As for the mTPU composites with a 90 : 10 (w/w) ratio of TPU : YIG, a small cylindrical pellet approximately 4.1 mm in length and 2.2 mm in diameter was weighed on the microbalance and then measured in the VSM with the magnetic field applied parallel to the pellet's axis. All samples were assembled in the VSM sample holder using Teflon tape. Due to the high magnetic moment of the samples, there was no need to correct for the diamagnetic response of the sample holder.

2.7. Magnetic actuation experiments

The mTPU samples were cut into two different shapes: a flower-like shape, 30 mm wide, and a 5 mm × 20 mm rectangular tape (Fig. 2a). Flowers and tapes were cut from compression-moulded sheets with two different thicknesses (500 μm and 150 μm). The applied magnetic field values (H) were estimated using a gaussmeter (FH-43, Magnet-Physik Dr Steingroever GmbH, Köln, GER), placed at the sample position, varying the distance of the permanent magnets, and by COMSOL Multiphysics®[51] simulations using the *Magnetic Fields* module (Fig. S4, ESI†).

For the actuation performance of the tapes, a cylindrical permanent magnet (NdFeB, N45 grade, ∅ 5 mm × 10 mm length), attached to an *xyz* stage (Creative Devices), was aligned with the top of the tape. The initial distance between the magnet and the tape was 15 mm, resulting in an H of 55 Oe. The magnet was moved along the *x*-axis, as schematized in Fig. 2b. H was >0.3 kOe for distances smaller than 5 mm. To test flower-shaped samples of different thicknesses, a cylindrical permanent magnet (NdFeB, N42 grade, ∅ 21 mm × 20 mm length) was attached to an *xyz* stage and aligned with the centre of the

flower. The initial distance was set to 45 mm (H = 0.114 kOe), and the magnet was moved along the *x*- and *z*-axes (Fig. 2c). At a distance of 2 cm, the H at the sample was ~0.5 kOe.

2.8. Simulations using COMSOL Multiphysics®

Magnetic flux density (B), magnetic deformation forces (F) and displacement (δ) of the rectangular tapes were simulated using the *Magnetic Fields* and *Solid Mechanics* modules of COMSOL Multiphysics®.[51] B was estimated for a cylindrical permanent magnet made of sintered NdFeB (N45 grade) with 5 mm diameter and 10 mm length. The resulting B values along the magnet's axis corroborate well with the measured ones, as a function of the distance to the magnet's end (Fig. S4, ESI†). Additional details on the simulations performed and the parameters used are presented in section 3 of the ESI.†

2.9. Electrical circuit switch actuator tests

Bi-layers of mTPU/Au were obtained by sputtering. A 25 × 25 mm film of mTPU with 500 μm thickness was placed in a sputtering chamber, with a base pressure of 3×10^{-7} mbar, a growing pressure (Ar) of 8.6×10^{-3} mbar and an Ar flux of 8 sccm.

A 5 × 20 mm tape of mTPU/Au was cut, and one end was attached to a metallic clip connected to one of the wires of the circuit. The other end of the tape was left in contact with the tip of an electrical wire (Au layer facing inwards to make the electrical contact) and free to move to open the circuit whenever a magnetic field was sufficient to deform the sample. A cylindrical permanent magnet (NdFeB, N45 grade, ∅ 5 mm × 10 mm length) attached to an *xyz* stage, was used to induce sample deformation. A standard laboratory direct current (DC) power supply was used to power the circuit (at 4 V) connected to a 12 V lamp bulb.

2.10. Statistical analysis and data presentation

Statistical analysis and data visualization were conducted using RStudio, version 4.2.3,[52] with dplyr,[53] tidyverse,[54] and ggplot[55] packages.

3. Results and discussion

## 3.1. Structure and morphology of YIG particles and composites

The X-ray diffraction (XRD) pattern of sol–gel-synthesised calcined YIG is shown in Fig. 3a. The pattern matches the $Ia\bar{3}d$ cubic crystal structure of YIG, with sharp garnet (420), (422), and (440) peaks. The material presents a small concentration of orthorhombic YFeO$_3$ (marked with an * in Fig. 3a).[56,57] The average crystallite size was determined according to Scherrer's equation (eqn (1)), using (420), (422), and (440) peaks. A grain size of 34 ± 1 nm was estimated for the YIG particles.

YIG phonon modes may be observed by Raman spectroscopy, namely, T$_{2g}$, E$_g$, and A$_{1g}$ modes.[59,60] Raman spectra acquired from 5 different zones of the YIG powder are presented in Fig. 3b. Peak attribution of the phonon modes was
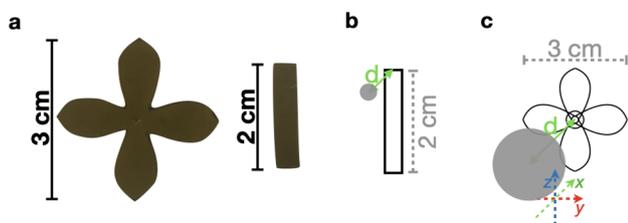
Fig. 2 (a) Photos of the 500 μm thick mTPU samples. Schematic representations of the actuation performance tests, where *d* is the distance between the tip of the magnet and the sample, illustrating two different magnet configurations: (b) aligned with the top of the tape sample, and (c) aligned with the centre of the flower-like sample.
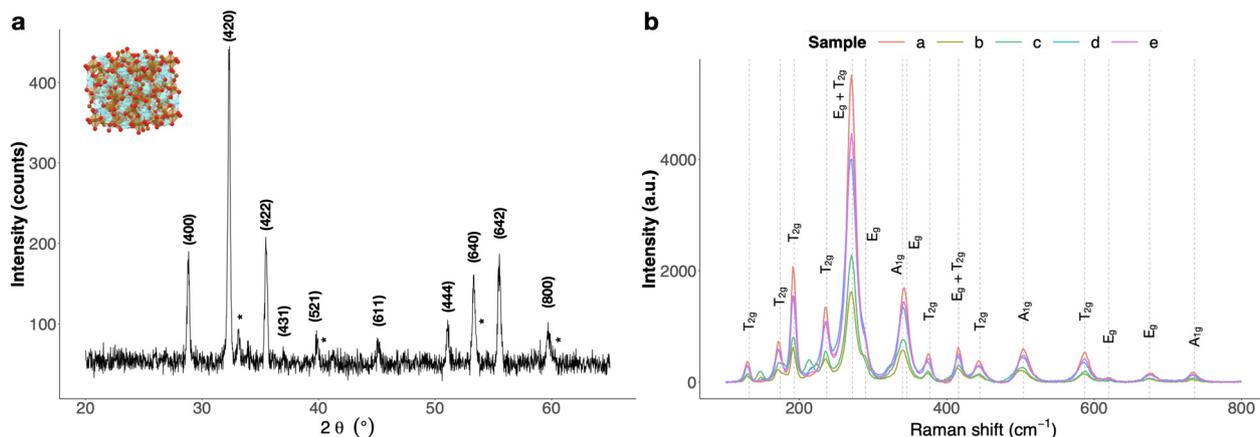
Fig. 3 (a) XRD patterns of sol–gel-synthesised YIG particles. Miller indices correspond to the YIG cubic structure, while peaks marked with an * correspond to orthorhombic $YFeO_3$. The inset illustrates the $Ia\bar{3}d$ crystal cubic structure of YIG (retrieved from the Materials Project for $Y_3Fe_5O_{12}$ (mp-4704) from database version v2023.11.1.[58]). (b) Raman spectra of sol–gel-synthesised YIG powder in five different zones of the sample (a to e). Vertical dashed lines indicate the characteristic Raman shifts of YIG.

based on works reported in the literature.[39,59,60] The observed Raman shifts correspond to the garnet phase of YIG; as expected, prominent peaks are found at ~270 cm^{-1}, ~190 cm^{-1}, ~340 cm^{-1}, and ~237 cm^{-1}. The Raman spectrum of the mTPU composite shown in Fig. S2† was recorded in the range of 100 to 800 cm^{-1}. YIG phonon modes are observed for mTPU, confirming that the YIG structure was not affected by the composite processing conditions.

Scanning electron micrographs show a porous coral-like structure for YIG powder, as depicted in Fig. 4a and b. Micrographs of mTPU (Fig. 4c and d) present differently sized agglomerates of YIG (from 2 μm up to 19 μm, Fig. S3†), with a good polymer/particle interface.

3.2. Thermal and thermomechanical composite characterisation

The thermograms illustrated in Fig. 5 reveal that the mTPU composites are thermally stable up to 284 °C (±2), about the same as melt-mixed TPU (286 °C ± 1). The degradation of TPU results in a ~1.6 wt% residue at 700 °C, whereas mTPU registers an average 12 wt% residue at the same temperature. Assuming that no other reactions occurred, the percentage of YIG can be estimated to be ~10.4 wt% (Fig. 5a). The degradation reaches its maximum rate at ~387 °C for the composites, measured as the temperature at the maximum of the first derivative of the TGA curve, which is 10 °C higher than that of pure TPU (Fig. 5b, Table 2).

The storage modulus (E') of the mTPU composites is higher than that of TPU (Fig. 6a, Table 3) above T_g and up to 70 °C. T_g, measured at the peak of tan δ (Fig. 6b), is about 4 °C lower for mTPU samples. Tan δ values are below 1, in the range of −80 °C to 150 °C, and are lower for mTPU (0.67, at maximum tan δ) than for TPU (0.79, at maximum tan δ), indicating a higher elastic response of the composite compared to the neat polymer. Energy absorption can be evaluated through the tan δ curve. At T_g, tan δ reaches its maximum; thus during the tran-
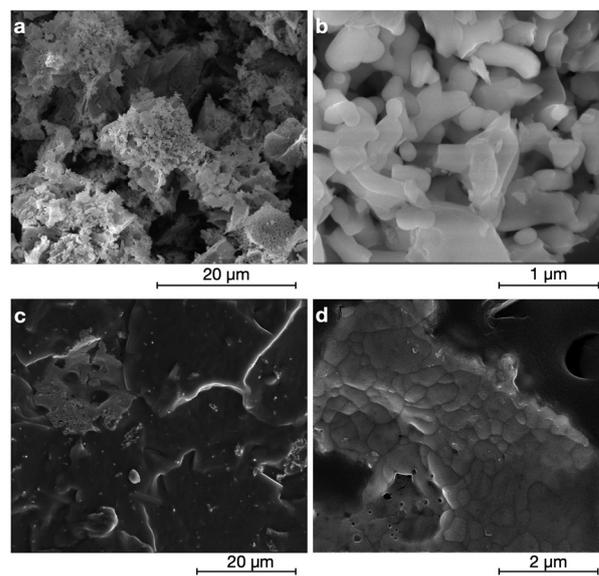

Fig. 4 Scanning electron micrographs (secondary electron mode) of (a and b) YIG particles and (c and d) mTPU composites, at different magnifications.

sition from the hard to rubbery state, the stress applied causes some molecules to exhibit viscous flow whilst others remain rigid, resulting in molecular friction and increased energy absorption.[61,62] The maximum damping is higher for TPU than for mTPU since the latter has a higher content of rigid domains due to the presence of YIG powder in the composite. Overall, the thermomechanical response of neat TPU and its composite, with *circa* 10 wt% YIG, is very similar.
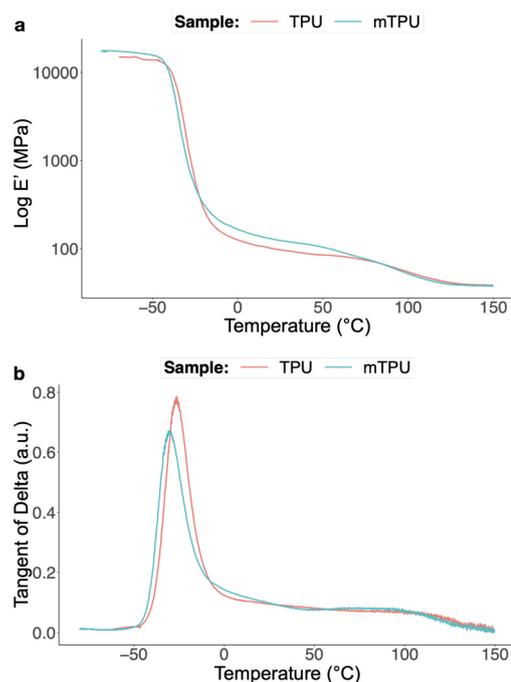
3.3. Magnetomechanical shape deformations

The magnetic hysteresis loop of YIG particles (Fig. 7, upper inset) and mTPU is shown in Fig. 7. A narrow loop, typical of soft magnets, is observed. The calculated magnetic mass in
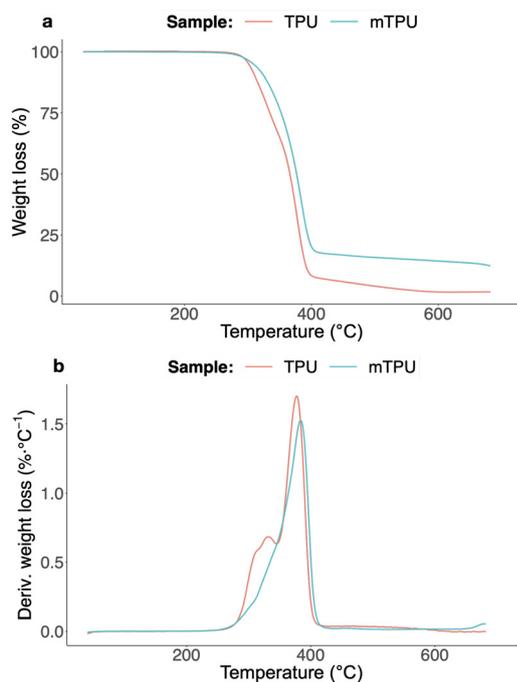
Fig. 5 Representative (a) thermograms and (b) derivative weight loss curves of TPU and mTPU.

Fig. 6 Representative thermomechanical curves of the (a) storage modulus (E') and (b) tan δ for neat TPU and mTPU.

Table 2 Residue at 700 °C (Res$_{700}$) and the temperature of maximum degradation rate (Peak$_{max}$), as determined through thermogravimetric analysis, for neat TPU and mTPU samples

Sample	Res$_{700}$ (%)	Peak$_{max}$ (°C)
TPU	1.6 ± 0.5	378 ± 5
mTPU	12 ± 1	387 ± 4

Table 3 Elastic modulus (E') at 0, 25, 37 °C, and T_g, determined through the tangent of delta (°C), for TPU and mTPU

Sample	E' (MPa)			T_g (°C)
	0 °C	25 °C	37 °C	
TPU	124.6 ± 0.2	96.3 ± 0.2	89.6 ± 0.4	−26.40
mTPU	164 ± 9	122 ± 7	113 ± 7	−30.07

the mTPU composite, taking into consideration a mass magnetization of 26.4 emu g^{-1} for the sol–gel-synthesised YIG particles (pH 2, calcined), is around 5%, revealing magnetic filler loss upon sample processing. Table 4 summarises the main properties of the mTPU composite and the respective YIG particles used as fillers.

Remanence is rather low (around 20% of the saturation magnetization); therefore, the composites will be able to switch polarity often, with the particles not sustaining any magnetic orientation. The coercivity (H_c) of the calcined YIG particles is 39 ± 2 Oe, while the mTPU composite presents an H_c of 36 ± 2 Oe. With this in mind, a system was designed to test mTPU as an actuator that can be activated with small magnets at short distances. Both the thickness and shape of the sample are expected to play an important role in the mechanism of shape deformation due to physical constraints, as the mass subject to the magnetic force and the degree of freedom allowed will differ. A flower-like shape, 30 mm wide, and a rectangular tape, 5 mm × 20 mm, were cut from mTPU sheets prepared with two different thicknesses (500 μm and 150 μm).
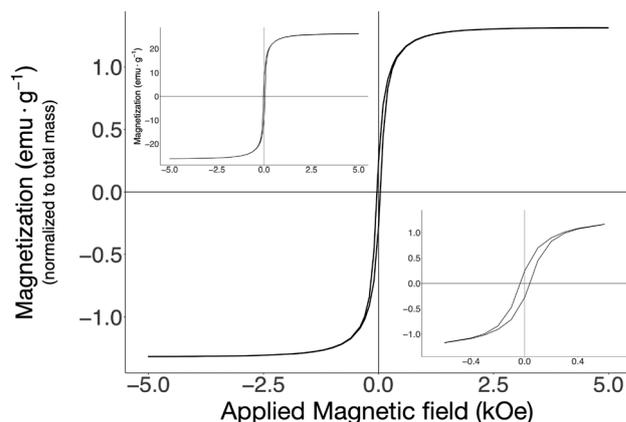
Fig. 7 Magnetic hysteresis loop of an mTPU cylindrical pellet with a total mass of approximately 14.7 mg. The lower inset shows a magnified hysteresis loop, from −0.7 to 0.7 kOe. The upper inset shows the hysteresis loop of the sol–gel-synthesised calcined YIG powder.

Table 4 Saturation magnetization (M_s, measured at 10 kOe, with an error of 0.1 emu g^{-1}), total mass (m, with an error of 0.001 mg), coercivity (H_c, with an error of 2 Oe) and reduced remanence ($m_r = \frac{M_r}{M_s}$, with an error of 0.01, where M_r is the remanent magnetization value) of the mTPU composite and the respective synthesised YIG powder filler

	M_s (emu g^{-1})	m (mg)	H_c (Oe)	m_r
mTPU	1.3	14.689	36	0.20
YIG filler	26.4	4.927	39	0.34

3.3.1. Rectangular tapes. The tape displacement is triggered by the approach of a magnet, as depicted in Fig. 8b and c, step 2, and Videos S1 and S2 (ESI†), for tapes with thicknesses of 500 and 150 μm, respectively.

The tape with 500 μm thickness has a lower bending angle than the one with 150 μm thickness due to its greater thickness. Withdrawing the magnet to its initial position allows the 500 μm thick tape to return to its original position (Fig. 8b, step 3). However, when the magnet returns to a 15 mm distance from the 150 μm thick tape, it still responds to a small H
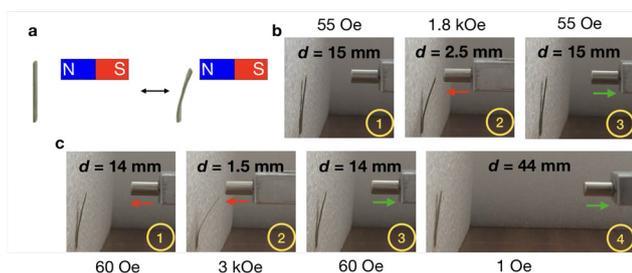

Fig. 8 (a) Illustration of the configuration used to test the rectangular tapes. Deformation of rectangular tapes of mTPU with (b) a thickness of 500 μm and (c) a thickness of 150 μm, upon the approach and withdrawal of a permanent magnet, where d is the distance between the tip of the magnet and the sample.

(55 Oe). Fig. 9a shows the results obtained for the maximum displacement (δ) of the upper end of the tape as a function of its distance (d) to the magnet. As expected, the thinner sample shows much higher δ values for similar d, and much higher sensitivity to the applied magnetic field, starting to bend at larger distances.

The bending of two rectangular tapes (5 × 20 mm) of the mTPU composite with different thicknesses (150 and 500 μm) was simulated using the *Solid Mechanics* module of COMSOL Multiphysics®. The tapes were divided into 3 sections: one fixed section of 2 mm in length (at the bottom), and two free sections of 16 and 2 mm in length at the middle and top part of the tape, respectively (Fig. 9c). To simulate the applied magnetic force (F) on the tape, we used the *Magnetic Fields, No Currents* module of COMSOL Multiphysics® at the upper section of the tape (top domain). Fig. 9b shows the results obtained as a function of the respective displacement, in which much higher forces (around 38 times higher) were needed to bend the thicker tape. F was applied at one of the lateral surfaces (boundary) of the upper section and perpendicular to it, as illustrated in Fig. 9c. Fig. 9a also shows the simulated results of δ as a function of d for both tape thicknesses. One should note that as the tape is bending and approaches the magnet, the magnetic field gradient increases, thus increasing the respective magnetic force acting on the tape. These simulations are just a simple approximation that does not consider such a change in magnetic force during the bending movement. Also, only the upper segment of the tape was used for the estimation and application of this constant magnetic force. Nonetheless, despite the small discrepancies found due to the approximations performed, the simulated results are still in good agreement with the experimental measurements.

3.3.2. Flower-like shape. The flower-like mTPU shape was tested with a stronger permanent magnet aligned with the centre of the flower. The results are presented in Fig. 10, for both thicknesses.
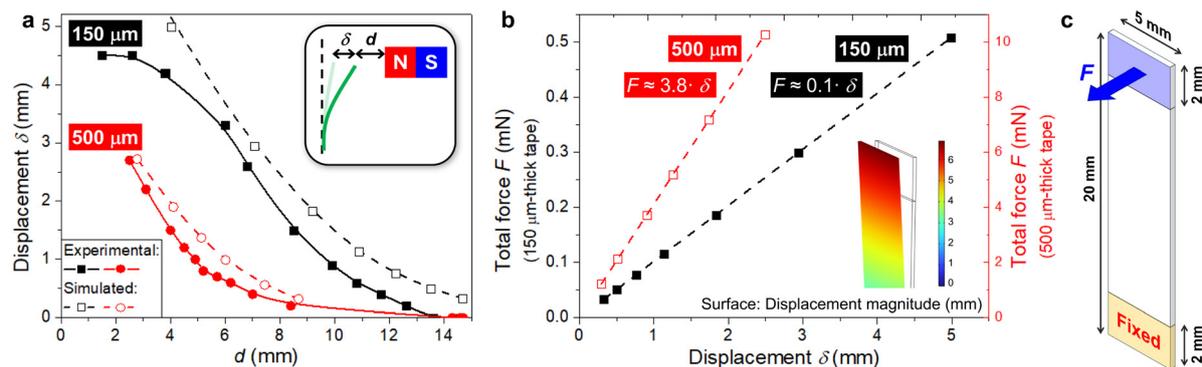
Fig. 9 (a) Maximum displacement (δ) of the upper end of the tape, as a function of its distance to the magnet (d) experimentally measured (closed symbols) and simulated using COMSOL (open symbols) for mTPU rectangular tapes with thicknesses of 150 (black) and 500 μm (red). Lines are guides to the eye. The inset shows a schematic representation of the bending of the sample with the magnet, evidencing the respective δ and d measurements. (b) COMSOL Multiphysics® simulation results, with respective linear fits, of the estimated total magnetic force F applied to the upper section of the tape as a function of the respective tape's displacement (δ). The inset shows a snapshot of a selected surface plot of the displacement magnitude. (c) Schematic representation of the simulated rectangular tape evidencing the fixed lower section and the total applied force F at the upper section.
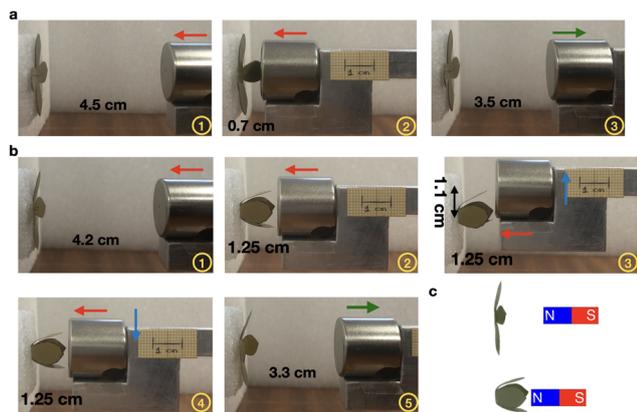
Fig. 10 Deformation of a flower-like shape (a) with a thickness of 500 μm and (b) with a thickness of 150 μm, upon the approach and withdrawal of a permanent magnet. (c) Illustration of the *petals'* movement.

Fig. 11 (a) SEM micrograph of the cross-section of the mTPU/Au bi-layer. (b) Digital microscope image of the actuator. (c) Top view of the magnetic switch configuration. Photos and schematic representations (insets) of the actuation process of an mTPU/Au-coated sample upon the approach of a magnet to (d) switch on and (e) switch off a lamp bulb. The red arrow points to the metal wire that is in contact with the mTPU/Au actuator (green arrow) when the circuit is closed.
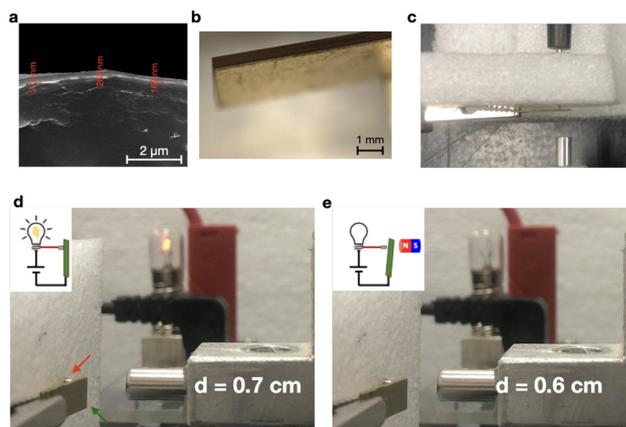
Upon the approach of the magnet, the flower with 500 μm thickness shows a small bending of the *petals* (Fig. 10a, step 2) which return to their initial position with the withdrawal of the magnet. The *petals* of the thinner flower bend completely (Fig. 10b, step 2) when subjected to an $H > 0.5$ kOe, at 1.25 cm magnet distance from the centre of the flower. Different bending angles of the *petals* can be achieved for different H intensities. Moreover, the vertical displacement of the magnet along the *z*-axis causes the central *petals* to move up and down, as depicted in Fig. 10b, steps 3 and 4, respectively. This phenomenon was also observed in the thinner tape (Video S3, ESI†).

Through these observations, we can conclude that the actuation mechanism relies on both: (i) attractive forces that arise from a magnetic field gradient, when the magnet approaches the samples, and (ii) torque created from the movement of the free-standing parts of the samples towards the magnet.

Compared to other magnetic TPU soft actuators that incorporate electrically insulating magnetic particles, the samples presented herein exhibit displacements at a low applied field (~85 Oe). Displacements at fields higher than 100 Oe are reported for TPU filled with hydrocarbon-modified $MnFe_2O_4$ nanoparticles, at weight percentages of 2, 4, 5 and 8,[37] and composites with 10 wt% of $Fe(CO)_5$ are reported to displace at 500 Oe.[34] It is important to acknowledge, however, that testing procedures are not standardised; thus, results must be compared carefully.

3.4. Magnetic switch actuator

Tapes with 500 μm thickness allow better control of the bending angle when subjected to an external magnetic field. Therefore, they were selected to produce bi-layers of mTPU/Au and to be tested as a switch component of a circuit, actuating under a magnetic field (Fig. S6†). The nanometric layer of Au presents good adhesion to mTPU, as observed through SEM

(Fig. 11a). The top and side views of the actuator are visible in Fig. 11b, evidencing the Au face. The bi-layer actuator was placed in the circuit with the Au layer facing inwards, in contact with the wire; when the permanent magnet is located at 0.7 cm from the sample, the Au face is in contact with the wire, hence the lamp is turned on (Fig. 11d). When the permanent magnet is moved 0.1 cm closer to the sample (0.6 cm distance from the sample), the sample bends towards the magnet, opening the circuit and turning the lamp off (Fig. 11e). It is possible to open/close the circuit without leaving residual magnetic interactions, maintaining a distance of 0.1 cm of approach and withdrawal to open and close the circuit.

4. Conclusions

The synthesis of cubic YIG, exhibiting a saturation magnetization of ~26 emu g^{-1}, with a crystallite size of ~34 nm, was achieved through a sol–gel method at pH 2 and after thermal treatment at 1000 °C. The resulting ferrimagnetic YIG particles were compounded with TPU, at a 10 wt% load, by melt mixing in a micro-compounder, without requiring the use of solvents. Notably, incorporating YIG particles did not cause significant changes to the thermal and mechanical properties of TPU. Good interfacial adhesion is observed between the polymer and the particles, suggesting good compatibility between the filler and polymer. These results show that micro-compounding is a suitable processing route to obtain homogeneous composites with a fair particle distribution.

The produced mTPU composites are soft magnets, capable of bending with the approach of a permanent magnet and returning to their original shape upon removal of the magnetic field, indicating reversible actuation capability. The magnetic

actuation effect was observed across various sample shapes, showcasing the ability of mTPU composites for controlled bending and displacement. This highlights the potential of this material, produced through solvent-free routes and without the need for intricate polymer processing techniques, to incorporate novel components in 3D-printed soft robotics. Additionally, a soft switch actuator, composed of an mTPU/Au bi-layer, was prepared and tested. The good compatibility between the nanometric Au layer and mTPU allows the bi-layer composite to effectively act as a switch, closing and opening the circuit under a small applied magnetic field.

Author contributions

M. M. S.: writing – original draft, visualization, data curation, formal analysis, funding acquisition, and investigation. A. R.: investigation. J. A. C.: writing – review and editing, funding acquisition, supervision, and verification. M. C. P.: conceptualization, writing – review and editing, funding acquisition, supervision, and verification. M. P. P.: conceptualization, writing – review and editing, funding acquisition, supervision, data curation, and verification.

Data availability

The authors confirm that the data supporting the findings of this study are available within the article and its ESI.†

Conflicts of interest

There are no conflicts to declare.

Acknowledgements

References

1 J. S. Leng, X. Lan, Y. J. Liu and S. Y. Du, *Prog. Mater. Sci.*, 2011, **56**, 1077–1135.

2 L. Hines, K. Petersen, G. Z. Lum and M. Sitti, *Adv. Mater.*, 2017, **29**, 1603483.

3 W. Zhao, L. W. Liu, F. H. Zhang, J. S. Leng and Y. J. Liu, *Mater. Sci. Eng., C*, 2019, **97**, 864–883.

4 C. Wischke, M. Behl and A. Lendlein, *Expert Opin. Drug Delivery*, 2013, **10**, 1193–1205.

5 W. M. Huang, C. L. Song, Y. Q. Fu, C. C. Wang, Y. Zhao, H. Purnawali, H. B. Lu, C. Tang, Z. Ding and J. L. Zhang, *Adv. Drug Delivery Rev.*, 2013, **65**, 515–535.

6 H. Gao, J. R. Li, F. H. Zhang, Y. J. Liu and J. S. Leng, *Mater. Horiz.*, 2019, **6**, 931–944.

7 C. Martín-Rubio, A. Rivelles, M. Schneider, J. C. D. Hoyo, V. Privitera, M. Worgull, M. Maicas and R. Sanz, *IEEE Trans. Magn.*, 2023, **59**, 1–6.

8 J. Shintake, V. Cacucciolo, D. Floreano and H. Shea, *Adv. Mater.*, 2018, **30**, 1707035.

9 O. V. Filippova, A. V. Maksimkin, T. Dayyoub, D. I. Larionov and D. V. Telyshev, *Polymers*, 2023, **15**, 2755.

10 J. Xu, X. Y. Wang, H. W. Ruan, X. R. Zhang, Y. M. Zhang, Z. H. Yang, Q. H. Wang and T. M. Wang, *Polym. Chem.*, 2022, **13**, 2420–2441.

11 S. Mondal, *Polym.-Plast. Technol. Mater.*, 2021, **60**, 1491–1518.

12 Y. H. Wu, Y. Wei and Y. Ji, *Polym. Chem.*, 2020, **11**, 5297–5320.

13 W. M. Huang, B. Yang, Y. Zhao and Z. Ding, *J. Mater. Chem.*, 2010, **20**, 3367–3381.

14 A. Kausar, *J. Plast. Film Sheeting*, 2020, **36**, 151–166.

15 M. M. da Silva, M. P. Proença, J. A. Covas and M. C. Paiva, *Micromachines*, 2024, **15**, 748.

16 M. Herath, J. Epaarachchi, M. Islam, L. Fang and J. S. Leng, *Eur. Polym. J.*, 2020, **136**, 109912.

17 H. M. Wang, Z. S. Zhu, H. Jin, R. Wei, L. Bi and W. L. Zhang, *J. Alloys Compd.*, 2022, **922**, 166219.

18 H. J. Chung, A. M. Parsons and L. L. Zheng, *Adv. Intell Syst.*, 2021, **3**, 2000186.

19 R. Mohr, K. Kratz, T. Weigel, M. Lucka-Gabor, M. Moneke and A. Lendlein, *Proc. Natl. Acad. Sci. U. S. A.*, 2006, **103**, 3540–3545.

20 M. Y. Razzaq, M. Anhalt, L. Frormann and B. Weidenfeller, *Mater. Sci. Eng., A*, 2007, **444**, 227–235.

21 Y. Cai, J. S. Jiang, Z. W. Liu, Y. Zeng and W. G. Zhang, *Composites, Part A*, 2013, **53**, 16–23.

22 H. Zou, C. Weder and Y. C. Simon, *Macromol. Mater. Eng.*, 2015, **300**, 885–892.

23 G. D. Soto, C. Meiorin, D. Actis, P. M. Zélis, M. A. Mosiewicki and N. E. Marcovich, *Polym. Test.*, 2018, **65**, 360–368.

24 G. D. Soto, C. Meiorin, D. G. Actis, P. M. Zélis, O. M. Londoõo, D. Muraca, M. A. Mosiewicki and N. E. Marcovich, *Eur. Polym. J.*, 2018, **109**, 8–15.

25 T. Calvo-Correas, A. Shirole, F. Crippa, A. Fink, C. Weder, M. A. Corcuera and A. Eceiza, *Mater. Sci. Eng., C*, 2019, **97**, 658–668.

26 S. Zhang, Y. B. Zhang, Y. H. Wu, Y. Yang, Q. M. Chen, H. Liang, Y. Wei and Y. Ji, *Chem. Sci.*, 2020, **11**, 7694–7700.

© 2025 The Author(s). Published by the Royal Society of Chemistry

RSC Appl. Polym., 2025, **3**, 865–874 | **873**

27 A. U. Vakil, M. Ramezani and M. B. B. Monroe, *Materials*, 2022, **15**, 7279.

28 X. H. Chen, X. Y. Zeng, K. Luo, T. Chen, T. Zhang, G. L. Yan and L. Wang, *Small*, 2022, **18**, 2205286.

29 A. Babaie, M. Rezaei, D. Razzaghi and H. Roghani-Mamaqani, *J. Appl. Polym. Sci.*, 2022, **139**, e5279.

30 M. Ramezani, E. E. Labour, J. J. Ji, A. U. Vakil, C. L. Du, T. K. Orado, S. Nangia and M. B. B. Monroe, *ACS Appl. Mater. Interfaces*, 2023, **15**, 56733–56748.

31 A. K. Bastola and M. Hossain, *Mater. Des.*, 2021, **211**, 110172.

32 C. P. Sanchez, C. J. Jerome, L. Noels and P. Vanderbemden, *ACS Omega*, 2022, **7**, 40701–40723.

33 P. R. Buckley, G. H. McKinley, T. S. Wilson, W. Small, W. J. Benett, J. P. Bearinger, M. W. McElfresh and D. J. Maitland, *IEEE Trans. Biomed. Eng.*, 2006, **53**, 2075–2083.

34 Y. Y. Wang, Q. Q. Guo, G. H. Su, J. Cao, J. Z. Liu and X. X. Zhang, *Adv. Funct. Mater.*, 2019, **29**, 1906198.

35 M. M. Schmauch, S. R. Mishra, B. A. Evans, O. D. Velevt and J. B. Tracy, *ACS Appl. Mater. Interfaces*, 2017, **9**, 11895–11901.

36 J. A. C. Liu, B. A. Evans and J. B. Tracy, *Adv. Mater. Technol.*, 2020, **5**, 2000147.

37 M. Yoonessi, J. A. Peck, J. L. Bail, R. B. Rogers, B. A. Lerch and M. A. Meador, *ACS Appl. Mater. Interfaces*, 2011, **3**, 2686–2693.

38 M. M. da Silva, J. A. Covas, M. C. Paiva and M. P. Proença, *Adv. Mater. Technol.*, 2025, 2401648.

39 E. J. J. Mallmann, A. S. B. Sombra, J. C. Goes and P. B. A. Fechine, *Solid State Phenomena*, 2013, **202**, 65–96.

40 A. Qureshi, A. Mergen and B. Aktas, International Conference on Superconductivity and Magnetism (ICSM), 2009, p. 012061.

41 M. Teirikangas, J. Juuti and H. Jantunen, *Compos. Struct.*, 2010, **93**, 179–183.

42 H. Soleimani, Z. Abbas, N. Yahya, K. Shameli and P. Shabanzadeh, *Int. J. Mol. Sci.*, 2012, **13**, 8540–8548.

43 H. K. Choudhary, R. Kumar, S. P. Pawar, A. V. Anupama, S. Bose and B. Sahoo, *ChemistrySelect*, 2018, **3**, 2120–2130.

44 C. B. Cheng, R. H. Fan, G. H. Fan, H. Liu, J. X. Zhang, J. X. Shen, Q. Ma, R. B. Wei and Z. H. Guo, *J. Mater. Chem. C*, 2019, **7**, 3160–3167.

45 I. Munaweera, A. Aliev and K. J. Balkus, *ACS Appl. Mater. Interfaces*, 2014, **6**, 244–251.

46 S. D. Figueiro, E. J. J. Mallmann, J. C. Goes, N. Ricardo, J. C. Denardin, A. S. B. Sombra and P. B. A. Fechine, *eXPRESS Polym. Lett.*, 2010, **4**, 790–797.

47 A. Sanida, S. G. Stavropoulos, T. Speliotis and G. C. Psarras, *J. Therm. Anal. Calorim.*, 2020, **142**, 1701–1708.

48 P. Vaqueiro and M. A. Lopez-Quintela, *Chem. Mater.*, 1997, **9**, 2836–2841.

49 T. T. N. Dao, N. P. Duong, T. Satoh, L. N. Anh and T. D. Hien, *J. Alloys Compd.*, 2012, **541**, 18–22.

50 S. H. Vajargah, H. R. M. Hosseini and Z. A. Nemati, *Mater. Sci. Eng., B*, 2006, **129**, 211–215.

51 *COMSOL Multiphysics®, v.62*, **https://www.comsol.com**, COMSOL AB, Stockholm, Sweden.

52 R. Team, *RStudio: Integrated Development Environment for R*, 2020, **https://www.rstudio.com/**.

53 H. Wickham, R. François, L. Henry and K. Müller, *dplyr: A Grammar of Data Manipulation, R package version 1.0.10*, **https://CRAN.R-project.org/package=dplyr**, 2022.

54 H. Wickham, M. Averick, J. Bryan, W. Chang, L. D. McGowan, R. François, G. Grolemund, A. Hayes, L. Henry, J. Hester, M. Kuhn, T. L. Pedersen, E. Miller, S. M. Bache, K. Müller, J. Ooms, D. Robinson, D. P. Seidel, V. Spinu, K. Takahashi, D. Vaughan, C. Wilke, K. Woo and H. Yutani, *J. Open Source Software*, 2019, **4**, 1686.

55 H. Wickham, *ggplot2: Elegant Graphics for Data Analysis*, Springer-Verlag, New York, 2016.

56 R. Pena-Garcia, Y. Guerra, D. M. Buitrago, L. R. F. Leal, F. E. P. Santos and E. Padron-Hernandez, *Ceram. Int.*, 2018, **44**, 11314–11319.

57 M. A. Musa, R. S. Azis, N. H. Osman, J. Hassan and T. Zangina, *Results Phys.*, 2017, **7**, 1135–1142.

58 A. Jain, S. P. Ong, G. Hautier, W. Chen, W. D. Richards, S. Dacek, S. Cholia, D. Gunter, D. Skinner, G. Ceder and K. A. Persson, *APL Mater.*, 2013, **1**, 011002.

59 K. S. Olsson, J. Choe, M. Rodriguez-Vega, G. Khalsa, N. A. Benedek, J. M. He, B. Fang, J. S. Zhou, G. A. Fiete and X. Q. Li, *Phys. Rev. B*, 2021, **104**, L020401.

60 W. H. Hsu, K. Shen, Y. Fujii, A. Koreeda and T. Satoh, *Phys. Rev. B*, 2020, **102**, 174432.

61 D. Sophiea, D. Klempner, V. Sendijarevic, B. Suthar and K. C. Frisch, *Interpenetrating Polym. Networks*, 1994, **239**, 39–75.

62 P. Kasprzyk, E. Sadowska and J. Datta, *J. Polym. Environ.*, 2019, **27**, 2588–2599.